Gonbad Kavous University

Journal of New Approaches in Water Engineering and Environment

Online ISSN: 2981-0280

Homepage: https://nawee.gonbad.ac.ir

Laboratory investigation of three-dimensional flow structure and local scour mechanisms around a novel spur dike with regular volumetric porosity (Chine blocks)

Mostafa Saberi Far[1], Seyed Amin Asghari Pari[2*]

[1]Department of Civil Engineering, Faculty of Engineering, Behbahan Khatam Alanbia University of Technology, Behbahan, Iran

Article Info

Article type:
Research Article

Received 23 December 2025

Revised 17 July 2026

Accepted 05 August 2026

Published online 22 December 2026

Keywords:

permeable spur dike

regular volumetric porosity

bleed flow

3D ADV

vorticity

local scour

ABSTRACT

Objective: To experimentally assess how regular, connected three-dimensional volumetric porosity modifies the hydrodynamic and morphodynamic response of a spur dike, and to compare a fully porous modular Chine dike and a three-row hybrid porous-shell configuration (3RC) with a conventional impermeable spur dike under submerged and non-submerged conditions.

Materials and Methods: Experiments were conducted in a 6.0 m long, 0.60 m wide recirculating flume at a flow depth of 0.15 m and discharge of 25.7 L/s. The approach flow was subcritical (U = 0.286 m/s, Fr approximately 0.23) and near the clear-water threshold (U/Uc = 0.96) over uniform non-cohesive sand with d50 = 1.2 mm. All dikes had a transverse length of 0.12 m. The Chine configuration was assembled from 2 x 2 x 2 cm cubic blocks with connected openings and a geometric volumetric porosity of approximately 0.25. Three-component velocities were measured using a Nortek Vectrino II ADV at 50 Hz for 120 s at each sampling node. Velocity records were despiked and filtered using correlation and SNR criteria. Each scour test continued for 24 h, and equilibrium bed topography was surveyed on a 1 x 1 cm grid with a laser profiler; dye and yarn tracers supported interpretation of the measured flow structures.

Results and Discussion: Regular volumetric porosity produced a controlled bleed flow through the dike body, relieved upstream stagnation pressure, weakened near-bed downflow, and reduced the concentration of high-vorticity cores near the structure. Under submerged conditions, porous configurations reduced peak near-bed downflow by about 50% relative to the solid case, while the fully porous Chine reduced peak vorticity at the dike by about 84%. Maximum equilibrium scour depth decreased from 9.3 cm for the solid dike to 7.1 cm for the fully porous Chine under submerged flow (23.7% reduction) and from 12.3 to 9.5 cm under non-submerged flow (22.8% reduction). The fully porous configuration also reduced scour-hole width and longitudinal extent and shifted the submerged deposition-bar onset from 23.2 to 14.95 cm, 35.6% closer to the structure. The 3RC case showed intermediate hydraulic and morphodynamic behavior.

Conclusion: A regular, hydraulically connected three-dimensional pore network can redistribute momentum through the structure, weaken coherent near-bed erosive motions, and reduce both scour depth and scour-hole extent. Within the tested conditions, the fully porous Chine configuration provided the most consistent scour mitigation, indicating that pore-network topology, in addition to overall permeability, is an important design variable for permeable river-training structures.

*Corresponding author, Email: asghari_amin@bkatu.ac.ir

Cite this article: Saberi Far, M., Asghari Pari, A. (2026). Laboratory investigation of three-dimensional flow structure and local scour mechanisms around a novel spur dike with regular volumetric porosity (Chine blocks). Journal of New Approaches in Water Engineering and Environment, 5(4), 19-47. https://doi.org/10.22034/nawee.2026.583195.1221.

© The Author(s).

Publisher: Gonbad Kavous University.

DOI: https://doi.org/10.22034/nawee.2026.583195.1221.

1. Introduction

Alluvial rivers continuously adjust their planform and cross-section through coupled erosion and deposition processes. To manage these morphodynamic changes, spur dikes (groynes) are extensively implemented as river-training structures. Their primary functions are to deflect the high-momentum flow core away from erodible banks, create sheltered recirculation zones for ecological habitats, and promote sediment deposition within groyne fields (Uijttewaal, 2005; Chakravarty et al., 2024). Despite their practical effectiveness in riverbank protection and navigation channel maintenance, the stability of these structures is frequently compromised by intense local scour around the upstream face and tip regions. This phenomenon remains a dominant failure mode and a critical design challenge, analogous to scour issues observed at bridge foundations (Melville, 1997; Melville & Coleman, 2000; Mashizi et al., 2025).

The hydrodynamic mechanism of local scour around conventional impermeable spur dikes is governed by complex, three-dimensional flow separation and boundary-layer dynamics (White, 2011). The obstruction of flow creates a near-stagnation region upstream and a strong adverse pressure gradient, which subsequently drives a downward velocity jet. This near-bed downflow rolls up to form a coherent horseshoe vortex system (HSV) that wraps around the structure. The HSV, combined with vigorous wake vortex shedding and shear-layer instabilities, substantially amplifies near-bed turbulence and bed shear stress, thereby accelerating sediment entrainment and scour whole development (Rajaratnam & Nwachukwu, 1983; Koken & Constantinescu, 2008a, b). Recent numerical and experimental investigations have further elucidated the critical role of these coherent structures across various boundary conditions, including non-submerged setups, differing approach-flow angles, channel bends, and varying bed roughness (Duan et al., 2009; Koken, 2011; Vaghefi et al., 2019; Pandey et al., 2020; Chen et al., 2022). Furthermore, local flow hydrodynamics and structural deformation around spur dikes can be significantly altered under complex environmental conditions, such as ice-covered channels (Jafari & Sui, 2024) or river confluences (Li et al., 2024).

Recent studies published in the Journal of New Approaches in Water and Environmental Engineering also emphasize the importance of predicting and mitigating local scour around hydraulic structures. Zahiri and Meftah (2023) showed that debris accumulation can intensify bridge-pier scour and proposed modified CSU-based dimensionless relationships for its prediction. Abdi Chooplou et al. (2022) reported that increasing the flow-drop height downstream of a Type-A trapezoidal piano key weir increases the maximum scour depth and alters downstream bed topography. More recently, Niknam et al. (2025) demonstrated experimentally and numerically that submerged plates can substantially reduce scour around spindle-shaped bridge piers. Together, these studies highlight the importance of controlled modification of near-bed flow and sediment transport, providing a relevant context for evaluating the regular three-dimensional porous spur-dike concept examined here.

To mitigate the destructive impacts of coherent turbulence structures, permeable spur dikes have emerged as a highly promising countermeasure (Hussein et al., 2025). By allowing a regulated portion of the discharge to pass through the structure (a process known as "bleed flow"), permeable designs effectively relieve the upstream stagnation pressure, diminish the intensity of the downflow jet, and moderate wake suction (Indulekha et al., 2023; Wang et al., 2023). Recent field and laboratory studies have demonstrated the morphodynamic benefits of nature-based and permeable interventions, such as bandal-like structures, in protecting river banks and modulating hydro-morphologic variations (Aung et al., 2023; Rahman et al., 2024; Ezzeldin et al., 2026). In parallel, a growing body of research has emphasized that the hydraulic effectiveness of permeable river-training structures depends not only on their overall permeability but also on the geometric arrangement of permeable elements and their interaction with the surrounding flow field (Teraguchi et al., 2008; Nath & Misra, 2017). Recent investigations have further demonstrated that geometric characteristics of permeable structures play a significant role in controlling local scour processes. For example, Khodakarami and Abbasi (2022) showed that the installation of permeable protective spur dikes upstream of conventional impermeable structures can effectively reduce local scour by modifying the near-bed flow field and dissipating flow energy. More recently, Hajiabadi et al. (2025) reported that, beyond the overall permeability ratio, the dimensions and configuration of openings substantially influence scour development around permeable spur dikes, highlighting the importance of internal flow pathways and hydraulic connectivity. Previous investigations have also shown that parameters such as opening size, spacing configuration, and internal flow connectivity can significantly influence momentum redistribution, turbulence generation, wake recovery, and local scour development (Pandey et al., 2020; Farshad et al., 2022). However, conventional permeable designs often exhibit significant limitations. For instance, structures with two-dimensional porosity (e.g., pile dikes) may generate concentrated jets through unfavorable spacing, leading to secondary localized scour, whereas structures utilizing random volumetric porosity (e.g., gabion spur dikes) possess irregular internal pore networks. This geometric irregularity makes their hydraulic response, wake dynamics, and ensuing scour hole morphology highly variable and difficult to parameterize (Al-Awadi et al., 2025).

Although the beneficial effects of permeability have been widely recognized, most previous studies have focused on permeability magnitude, spur-dike orientation, spacing arrangement, or global hydraulic response. Comparatively less attention has been devoted to the influence of pore-network architecture and the degree of geometric regularity within the permeable body. Available evidence suggests that structures possessing similar overall permeability may exhibit substantially different flow patterns and scour responses depending on the organization and connectivity of their openings. This observation highlights the need for permeable concepts

whose internal geometry can be systematically characterized, hydraulically parameterized, and directly linked to hydrodynamic and morphodynamic processes.

While recent advancements in hybrid ensemble models have improved the predictive capability of scour depth around spur dikes (Singh & Minocha, 2025), robust scour mitigation and accurate physical modeling still require permeable geometries that can systematically and reproducibly suppress near-bed coherent structures. Comprehensive reviews indicate that an ideal spur dike design should function as a distributed energy dissipator without introducing new localized scour triggers (Hussein et al., 2025). Therefore, there is a distinct motivation to develop permeable concepts featuring mathematically regular, connected 3D porosity. Such structures would not only be more amenable to scaling and hydraulic characterization but could also efficiently redistribute momentum, transferring energetic turbulence to smaller scales for enhanced dissipation. Despite this need, quantitative experimental evidence linking regular 3D volumetric porosity to the evolution of three-dimensional flow structures, vorticity fields, and equilibrium bed morphology remains fundamentally scarce.

To address this knowledge gap, the present study introduces and comprehensively evaluates a novel, modular spur dike constructed from "Chine" blocks, which form a regular, connected 3D volumetric pore network. Utilizing high-resolution Acoustic Doppler Velocimeter (ADV) measurements and precise laser topography, the specific objectives of this research are to: (i) quantify the hydrodynamic impact of regular volumetric porosity on near-bed downflow, vorticity magnitude, and wake recovery; (ii) characterize the three-dimensional mean flow patterns and relate them to the mechanisms governing equilibrium scour morphology; and (iii) comparatively assess the hydraulic and morphodynamic performance of a fully porous Chine spur dike and a hybrid three-row porous shell configuration against a conventional impermeable reference under both submerged and non-submerged conditions.

2. Materials and methods

2.1. Flume, flow conditions, and sediment

Experiments were conducted in a recirculating rectangular flume with transparent glass sidewalls at the Hydraulics Laboratory of Khatam Alanbia University of Behbahan (Iran). The test section is 6.0 m long, B = 0.60 m wide, and maintained at a flow depth of h = 0.15 m. The channel aspect ratio was B/h = 4. Although larger aspect ratios are often recommended for ideal two-dimensional open-channel flow, previous experimental investigations of isolated spur dikes have demonstrated that aspect ratios greater than approximately 3 are generally sufficient to avoid dominant sidewall interference in the near-field region surrounding the structure. Moreover, the relatively small blockage ratio employed in the present study (L/B = 0.20) minimized interaction between the spur-dike-induced flow field and the opposite wall. Since

all configurations were tested under identical hydraulic conditions, any residual sidewall effects were systematic and did not affect the comparative conclusions of this study. Discharge (Q=25.7 L/s) was regulated by a centrifugal pump coupled with a gate valve and monitored using an electromagnetic flowmeter with an accuracy of ±0.1 L/s. The discharge (Q = 25.7 L/s) was selected to maintain subcritical flow conditions (Fr ≈ 0.23) while achieving a flow intensity of U/Uc = 0.96. This near-threshold condition was intentionally chosen because previous studies have shown that maximum clear-water scour typically develops when the approach velocity is close to the critical sediment entrainment velocity (Melville, 1997).

To prevent bed armoring and ensure uniform scour development, non-cohesive uniform sand with a median grain size of d50=1.2 mm and a geometric standard deviation of σg=1.41 (σg<1.5) was utilized (Raudkivi & Ettema, 1983). All experiments were performed under near-threshold clear-water conditions (U/Uc=0.96, where U is the approach flow velocity and Uc is the critical velocity for sediment entrainment). This specific flow intensity was selected as it is widely documented to produce the maximum equilibrium scour depth around instream structures (Melville, 1997). Each experimental run was conducted continuously for 24 h. The evolution of maximum scour depth was periodically monitored during the tests. Following commonly adopted equilibrium criteria in clear-water scour studies, equilibrium conditions were assumed when the variation in maximum scour depth remained less than 1 mm during a consecutive three-hour observation period. The selected test duration and criterion are consistent with the recommendations of Melville and Chiew (1999) and ensure that the reported scour depths represent equilibrium values. A summary of the hydraulic and sediment parameters is provided in Table 1.

Prior to the experiments, velocity measurements were performed at several consecutive cross-sections along the approach reach to verify flow development. The measured velocity profiles exhibited negligible variations between adjacent sections, confirming that fully developed approach-flow conditions were achieved before the flow reached the test section.

Table 1- Hydraulic and sediment conditions for the experiments.

Parameter	Value/Description	Rationale / Reference
Discharge, Q	25.7 L/s	Selected to ensure subcritical approach flow and near-threshold clear-water scour conditions.
Flow depth, h	15 cm	Maintains an appropriate blockage ratio and stable free-surface condition.
Mean approach velocity, U	0.286 m/s	Calculated from U = Q/(Bh).
Froude number, Fr	≈ 0.23	Indicates subcritical flow condition, Fr = U/(gh)^0.5.
Reynolds number, Re	≈ 4.3 × 10⁴	Indicates fully turbulent approach flow, Re = Uh/ν.
Median sediment size, d50	1.2 mm	Non-cohesive, relatively uniform sediment to minimize bed armoring effects.
Geometric standard deviation, σg	1.41	Uniform sediment condition, σg < 1.5.
Flow intensity, U/Uc	0.96	Near-threshold clear-water condition; maximum scour commonly occurs near this range.
Test duration	24 h	Selected to ensure development of equilibrium scour conditions.

2.2. Spur dike configurations

Three distinct spur dike configurations were investigated (Fig. 1):

- Impermeable spur dike (Solid): Constructed from waterproofed wood with a thickness of 2 cm, serving as the baseline reference case.
- Fully porous spur dike (Chine): A novel modular structure assembled from cubic blocks (2×2×2 cm).
- Three-row hybrid Chine (3RC): A composite configuration featuring a solid inner core surrounded by an outer porous shell comprising three layers of Chine blocks.

Each Chine block measured 2 × 2 × 2 cm and contained circular openings with diameters of 0.9 cm on all faces, generating a connected three-dimensional pore network with a geometric volumetric porosity of approximately $\phi = 0.25$. The characteristic pore diameter was approximately 7.5 times larger than the median sediment size (d50 = 1.2 mm), preventing pore blockage during the experiments. It should be noted that, as with all laboratory-scale porous structures, some scale effects associated with Reynolds-number similarity may exist. However, the present work is primarily intended to investigate the comparative hydrodynamic and morphodynamic mechanisms induced by regular volumetric porosity under controlled hydraulic conditions. Assessment of prototype-scale behavior and permeability scaling remains an important topic for future studies.

The transverse length of all spur dike models was fixed at L=0.12 m. This specific blockage ratio (L/B=0.20) was selected to represent an isolated structure, generating distinct flow separation and wake dynamics without inducing excessive hydrodynamic interaction or flow contraction against the opposite flume wall (Koken & Constantinescu, 2008a; Chen et al., 2022). To comprehensively evaluate their performance, tests were conducted under both non-submerged and submerged flow conditions.

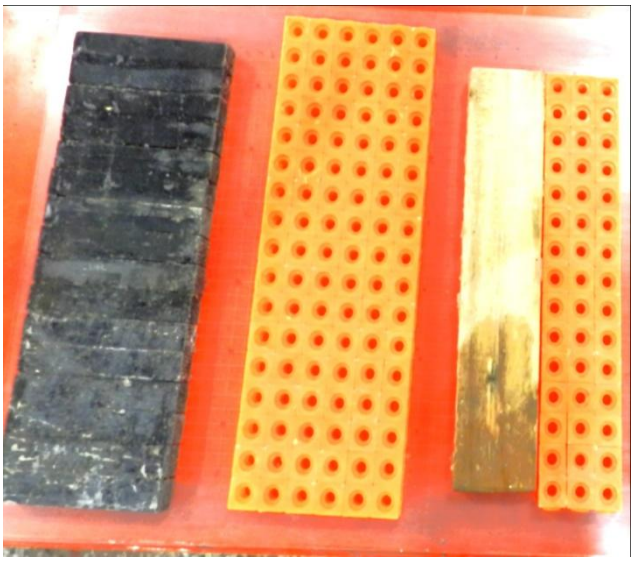

Figure 1- Spur-dike models tested in the laboratory flume (from left to right): impermeable (solid) spur dike, fully porous spur dike (Chine), and a three-row porous Chine spur dike (3RC)

2.3. Velocity measurements (ADV) and data processing

Instantaneous three-dimensional velocity components (u, v, w) were acquired using a Nortek Vectrino II Acoustic Doppler Velocimeter (ADV) equipped with a down-looking probe, operating at a sampling frequency of 50 Hz. At each measurement node, data were recorded for 120 seconds to guarantee the statistical convergence of both mean velocities and higher-order turbulence statistics (Buffin-Bélanger & Roy, 2005).

To ensure high-quality ADV measurements, raw velocity records were processed using the phase-space despiking algorithm of Goring and Nikora (2002). Additionally, samples with acoustic correlation values below 70% or signal-to-noise ratios (SNR) below 15 dB were discarded. The filtered datasets were subsequently used to calculate mean velocity components and derived quantities, including vorticity fields. These procedures minimize contamination caused by acoustic interference, particularly near the sediment bed and porous boundaries. The post-processed datasets were utilized to compute time-averaged mean velocities (U, V, W) and to derive spatial gradients, such as vorticity fields, employing a central-difference numerical scheme. Measurements were conducted across a structured, non-uniform grid (Table 2), which was strategically refined near the spur-dike tip, within the shear layer, and inside the scour hole to accurately capture high-gradient flow dynamics.

Table 2- ADV sampling grid and measurement locations (horizontal planes above the bed, longitudinal sections, and cross-sections relative to the spur dike).

Section type	Locations / distances (relative to bed, inner bank, and spur dike)
Horizontal planes (distance above bed)	0.5 cm, 2 cm, 5 cm, 7 cm
Longitudinal sections (streamwise direction, referenced to the inner bank)	6 cm, 9 cm, 12 cm, 15 cm
Cross-sections across the flume	5 cm upstream of the spur dike, at the dike, and 5 cm downstream of it

2.4. Bed topography and flow visualization

After each run, the flume was drained slowly to prevent bed collapse. Bed elevation was surveyed using a laser bed profiler (vertical accuracy ±0.5 mm) on a 1×1 cm grid. Digital elevation models were processed to extract the maximum equilibrium scour depth ds, scour-hole dimensions, and deposition-bar metrics. Dye injection and yarn tracers were used to visualize flow pathways and coherent structures, thereby supporting the interpretation of the ADV results (Fig. 2).

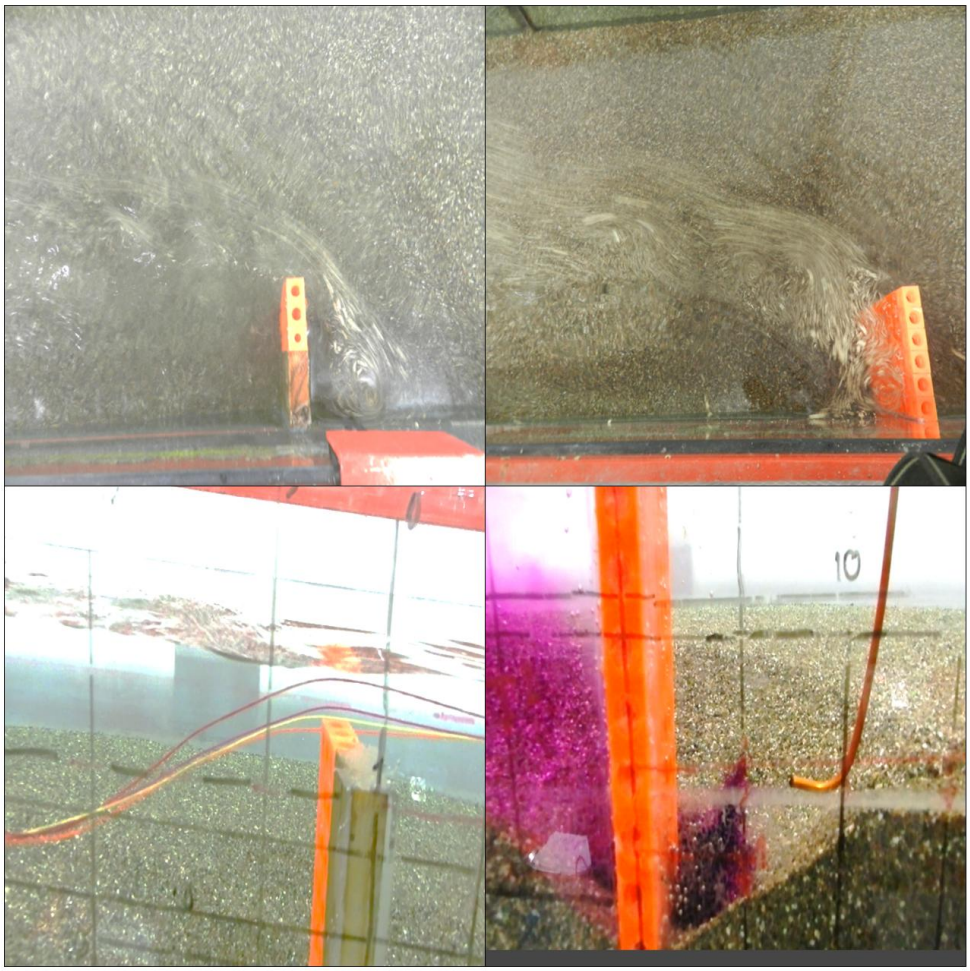

Figure 2-Representative flow-visualization snapshots using dye injection and yarn tracers to identify near-field flow patterns around the spur dikes.

2.5. Dimensional analysis

Considering the equilibrium scour depth (ds) as the dependent variable, the governing parameters may be expressed as:

ds = f(U, Uc, h, L, B, d50, g, ρ, μ) (1)

Applying the Buckingham Π theorem yields:

ds/h = f(U/Uc, Fr, L/h, B/h, d50/h, Re) (2)

where Fr = U/(gh)^0.5 and Re = Uh/ν.

Since all experiments were performed under identical hydraulic and sediment conditions, variations in scour morphology are primarily attributable to differences in spur-dike permeability and porosity topology.

3. Results and discussion

A reference velocity was used for non-dimensional comparisons:

$$U_0 = \frac{Q}{Bh} = \frac{0.0257}{0.60\times0.15} = 0.286 \text{ m s}^{-1} \quad (3)$$

Two indices are used for lateral and vertical peak magnitudes:

$$I_V = \frac{\max|V|}{U_0}, I_W = \frac{\max|W|}{U_0} \quad (4)$$

To facilitate interpretation of the measured velocity fields and their linkage to scour morphology, the flow is discussed using three complementary frameworks. First, the transverse turbulent-momentum transfer concept and its associated Dike Field Zone (DFZ), Mean Exchange Zone (MEZ), and Mean Stream Zone (MSZ) are adopted as a reference for describing momentum redistribution around a spur dike (Fig. 3). Second, based on dye/yarn visualizations, the near-field flow is qualitatively subdivided into distinct regions under non-submerged and submerged conditions (Fig. 4), which are used to interpret differences in separation, recirculation, and wake recovery among configurations. Third, the ADV measurement layout and the adopted classification of sampling points inside the scour hole (H) and outside the scour hole (F) are defined according to Fig. 5 and used consistently in the contour and profile comparisons presented below.

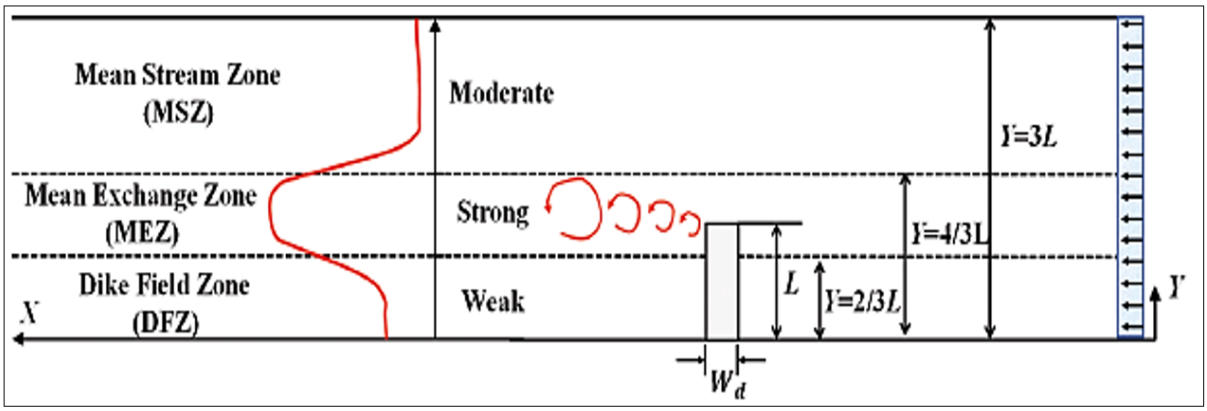

Figure 3- Schematic of transverse turbulent-momentum transfer and flow zones around a single impermeable spur dike (DFZ, MEZ, MSZ), adapted from Chen et al. (2022).

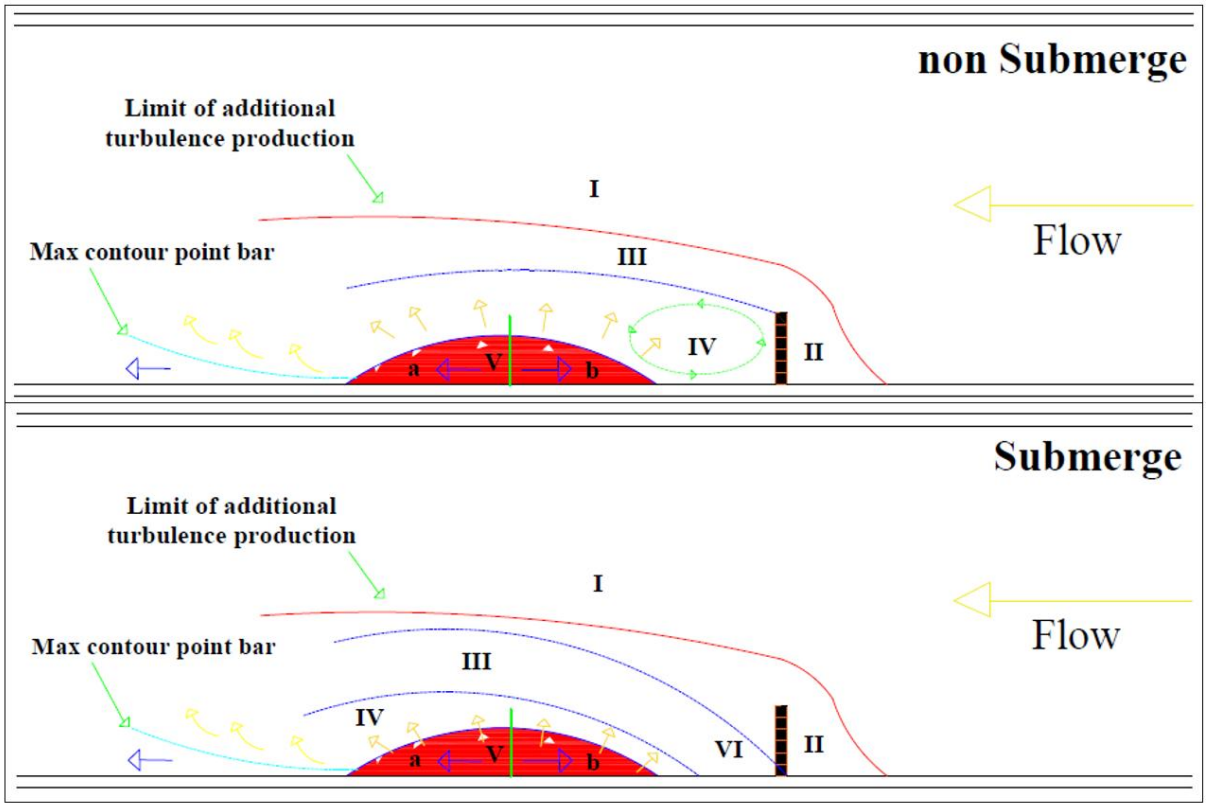

Figure 4-Flow-region delineation based on visual observations for (a) non-submerged and (b) submerged spur-dike conditions.

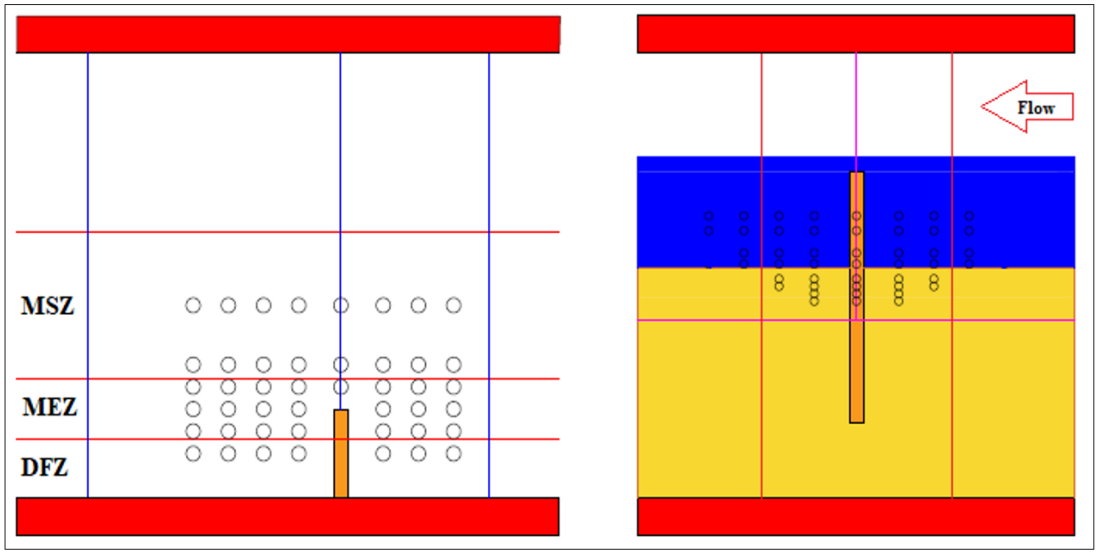

Figure 5- Locations of ADV velocity measurements and adopted region classification (H: inside the scour hole; F: outside the scour hole), shown in plan and side views.

3.1. Streamwise velocity U and momentum distribution

The streamwise velocity component U controls momentum redistribution, shear-layer development, and wake recovery, and therefore plays a primary role in scour initiation and

growth. In what follows, near-bed contours (Fig. 6; horizontal plane $z = 0.5$ cm above the bed) are interpreted using the DFZ–MEZ–MSZ zonation framework (Fig. 3) together with the flow-region delineation derived from dye/yarn visual observations (Fig. 4). The blue line in Fig. 6 marks the maximum transverse extent of the equilibrium scour hole; accordingly, sampling locations are classified as H (inside the scour hole) and F (outside the scour hole) following the definition in Fig. 5.

Solid spur dike: A sharp velocity gradient forms between the main stream (MSZ) and the near-field separation/recirculation region (DFZ/MEZ), indicating a strong free shear layer consistent with the conceptual transverse momentum-transfer pattern in Fig. 3. A pronounced negative-velocity core$U$ in the sheltered region indicates a marked pressure deficit and coherent wake circulation, in agreement with the recirculation features identified under submerged conditions (Fig. 4). The strong blockage effect intensifies near-field exchange between MSZ and MEZ (Fig. 3), which is typically associated with elevated near-bed turbulence levels and enhanced scour potential.

Fully porous Chine: The streamwise-velocity field becomes smoother$U$ and more spatially distributed. The connected regular volumetric porosity enables a controlled bleed flow through the structure, injecting momentum into the wake and reducing the magnitude of wake suction. This corresponds to a weaker separation/recirculation signature relative to the solid case and is consistent with the region boundaries inferred from Fig. 4. The reduced contrast between DFZ/MEZ and MSZ (Fig. 3) indicates more distributed momentum exchange, compatible with the observed reduction in equilibrium scour depth (Figs. 16–17).

3RC: The response is intermediate between the solid and fully porous cases. Local suction and accelerated pathways may occur within the porous shell as the flow preferentially enters the lower-resistance outer layer before interacting with the inner solid core. As a result, a recirculation core persists but is weaker than in the solid case, indicating partial damping of separation dynamics by the porous envelope. This partial mitigation aligns with the mixed near-field pattern suggested by Fig. 4 and the H/F-based comparison framework in Fig. 5, and is reflected in the intermediate scour reduction (Figs. 16–17).

Overall, increasing porosity shifts the flow response from “strong blockage–strong separation” toward “controlled leakage–distributed momentum exchange” (Fig. 3), consistent with the reduced equilibrium scour depth observed for the porous configurations (Figs. 16–17).

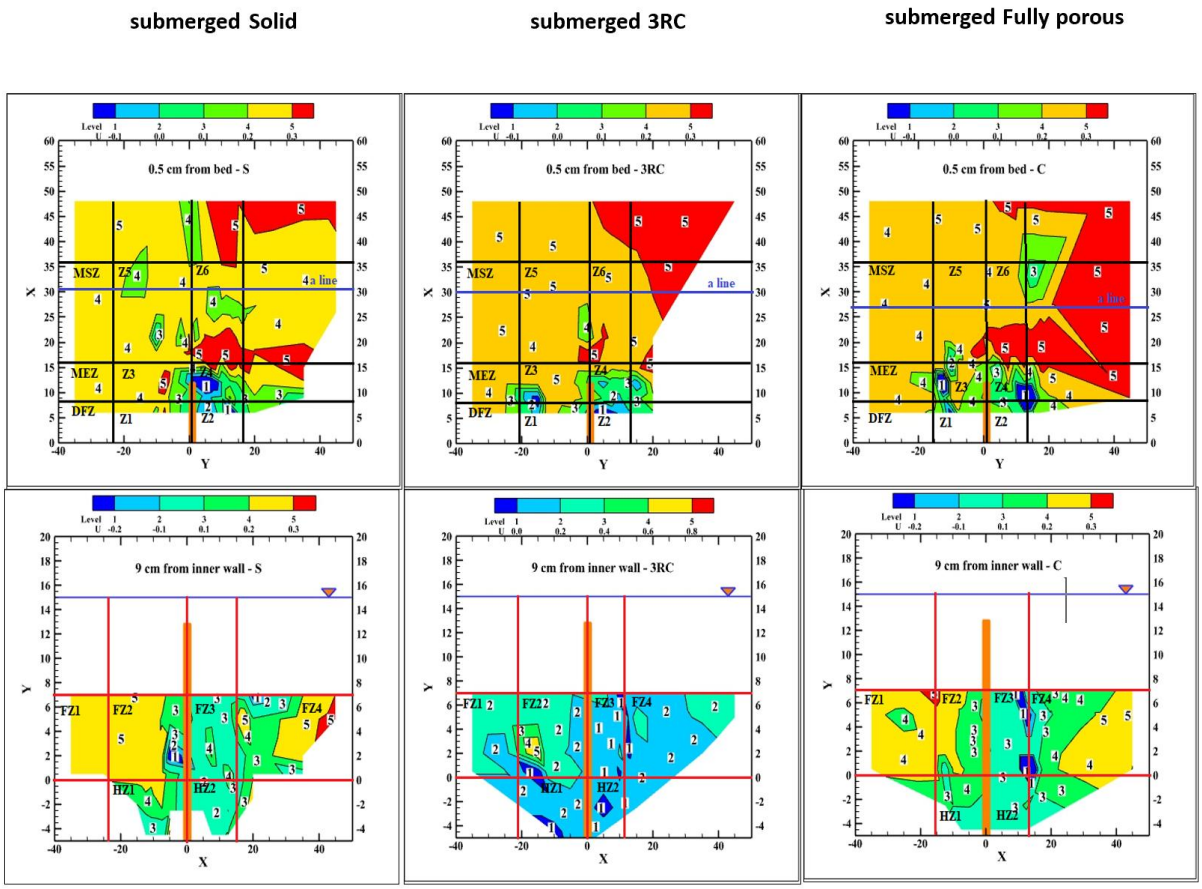

Figure 6-Streamwise velocity (U) contours for submerged runs at $z = 0.5$ cm above the bed and at 9 cm from the inner bank (blue line a indicates the maximum scour-hole width in the transverse direction).

3.2. Lateral velocity V and flow deflection (submerged)

The lateral velocity component V governs flow deflection and the transverse exchange of momentum between the main stream and the dike field. To quantify the intensity of lateral deflection, a non-dimensional index is defined as

$$I_V = \frac{\max(|V|)}{U_0} \tag{5}$$

where $U_0 = 0.286$ m s^{-1} is the reference approach velocity.

On-dike section (Fig. 7, top). The impermeable (solid) spur dike exhibits the strongest lateral deflection, with max(|V|) ≈ 0.40 m s^{-1}, yielding $I_V \approx 1.40$. In contrast, the three-row hybrid Chine (3RC) reduces the peak to max(|V|) ≈ 0.10 m s^{-1} ($I_V \approx 0.35$; ~75% reduction), while the fully porous Chine reaches max(|V|) ≈ 0.20 m s^{-1} ($I_V \approx 0.70$; ~50% reduction).

Section at y = 12 cm from the inner wall (Fig. 7, bottom). The solid case attains max(|V|) ≈ 0.60 m s^{-1}, corresponding to $I_V \approx 2.10$. Both porous configurations show markedly weaker lateral velocities, with max(|V|) ≈ 0.20 m s^{-1} ($I_V \approx 0.70$), i.e., an approximate 67% reduction relative to the solid spur dike. Overall, permeability leads to a more distributed transverse momentum exchange and mitigates concentrated lateral shear in the near wake.

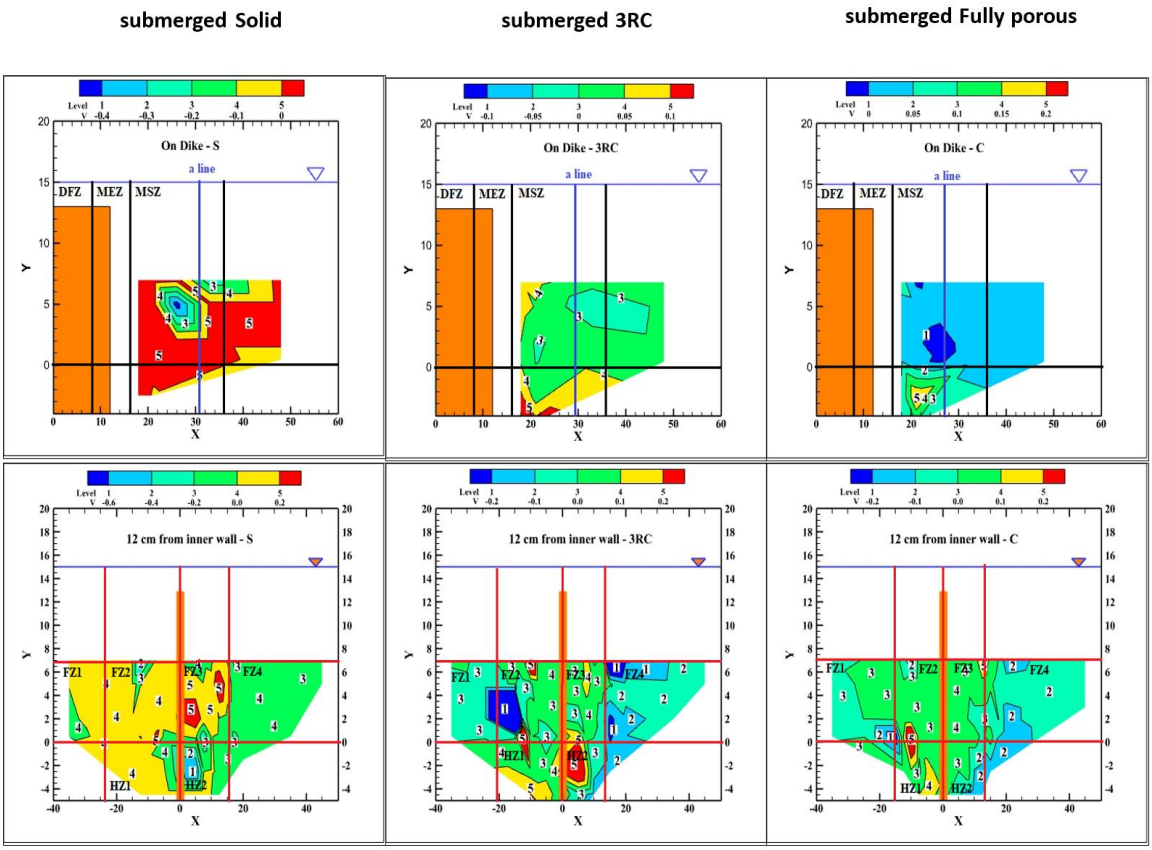

Figure 7- Lateral velocity (V) contours under submerged conditions: (top) on-dike section and (bottom) section at 12 cm from the inner bank, comparing solid, 3RC, and fully porous Chine cases.

3.3. Vertical velocity W, near-bed downflow, and implications for HSV-driven scour (submerged)

Near-bed downflow (negative W) is a primary driver of the horseshoe vortex system (HSV) development and scour initiation at spur dikes. The vertical-velocity maps in Fig. 8 (horizontal plane at z = 2 cm above the bed; sections at x = ±5 cm relative to the spur-dike location) indicate a systematic weakening of downflow as porosity increases. Using the non-dimensional index $I_W = \max(|W|)/U_0$ with $U_0 = 0.286$ ms^{-1}, the peak downward velocities are:

- Solid: $W_{\min} \approx -0.10$ m/s $\Rightarrow I_W \approx 0.35$
- 3RC and fully porous: $W_{\min} \approx -0.05$ m/s $\Rightarrow I_W \approx 0.17$

Accordingly, the porous configurations reduce the magnitude of near-bed downflow by approximately 50% compared with the impermeable (solid) spur dike. For the fully porous Chine, a portion of the upstream stagnation pressure is relieved through a distributed bleed flow within the connected pore network, thereby limiting the conversion of pressure head into an intense downward jet at the dike nose. For the 3RC configuration, the porous outer shell similarly diverts part of the incoming momentum into the porous layer, reducing the momentum available to strengthen HSV-related downflow near the bed. These trends are consistent with the observed reductions in equilibrium scour depth (Figs. 16–17).

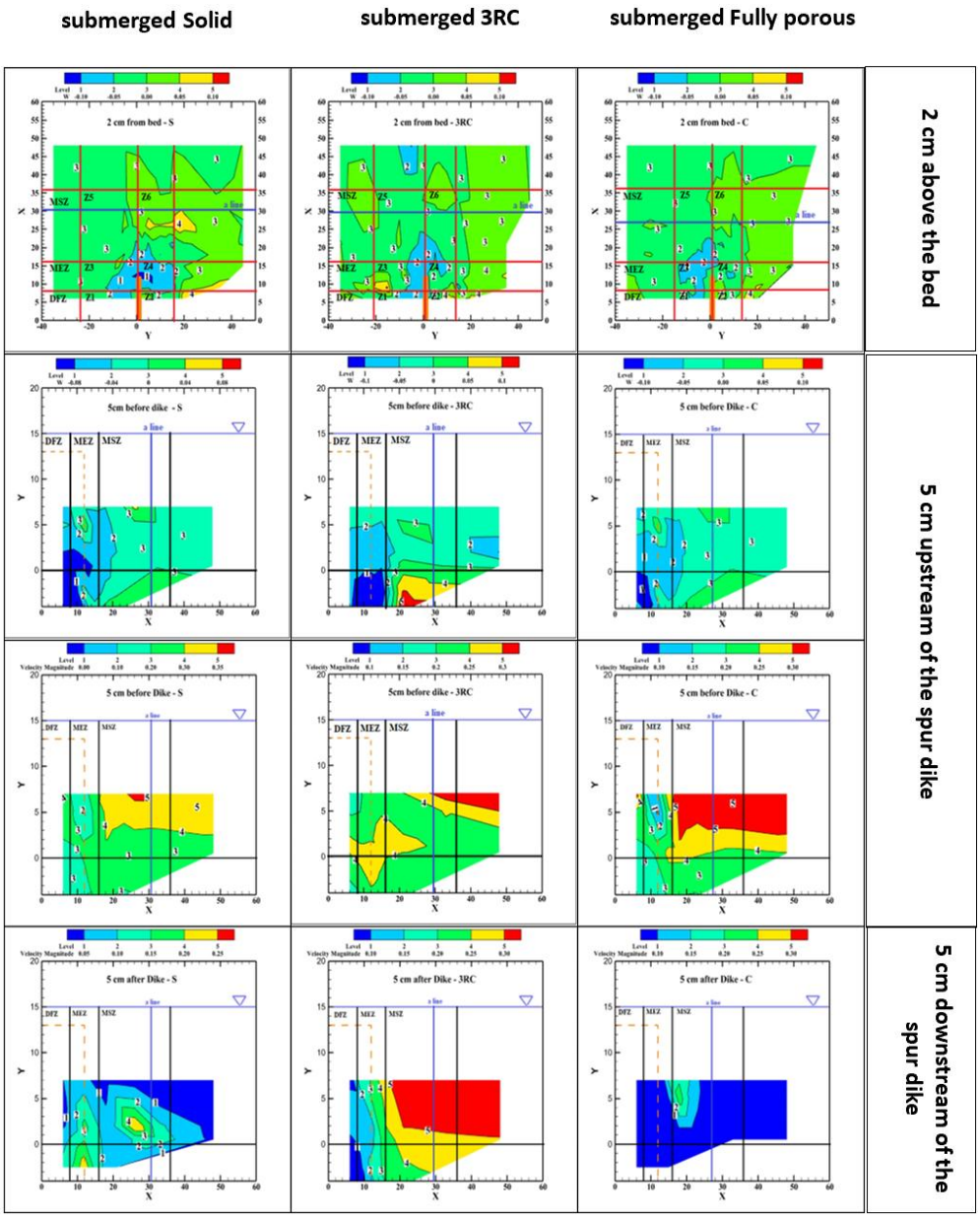

Figure 8-Vertical velocity (W) contours under submerged conditions at $z = 2$ cm above the bed, 5 cm upstream and 5 cm downstream of the spur dike.

3.4. Streamlines and flow topology

Streamline patterns (Fig. 9) highlight systematic differences in flow topology. In the solid case, strong streamline convergence at the nose and rapid divergence in the wake indicate energetic separation and intense vortex dynamics, consistent with an unstable wake and strong recirculation. In contrast, the porous and 3RC cases show smoother streamlines with milder convergence/divergence, indicating improved pressure recovery and reduced coherence of large-scale wake structures. This agrees with the reduced peak $|V|$ and $|W|$ reported in Sections 3.2–3.3.

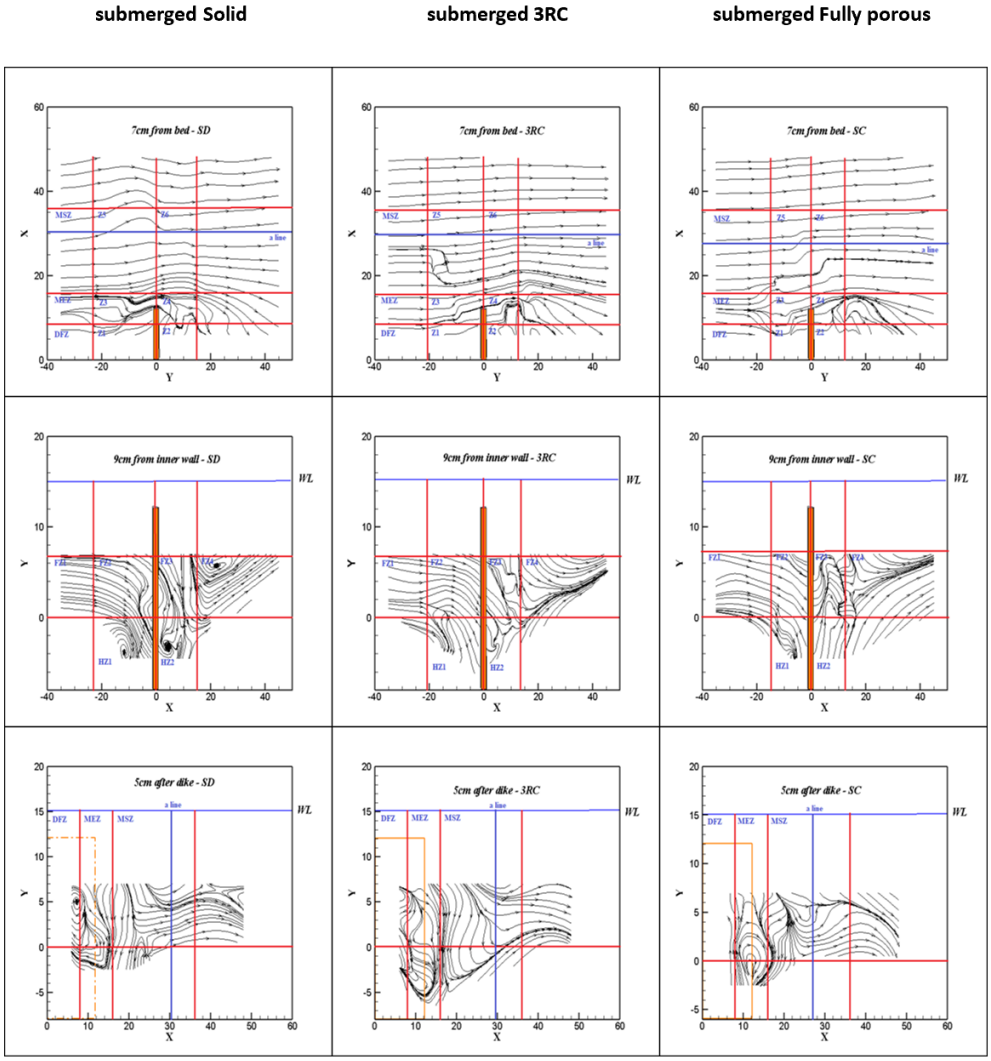

Figure 9- Streamline patterns under submerged conditions for selected planes, comparing solid, 3RC, and fully porous Chine cases.

3.5. Vorticity magnitude and attenuation of coherent rotation

Vorticity magnitude provides a direct measure of rotation intensity and erosive capacity. From Fig. 10 (maximum vorticity before, at, and after the spur dike), approximate values are:

- Upstream (+5 cm): solid $\omega_{max} \approx 0.32$, 3RC ≈ 0.13, fully porous ≈ 0.13 (~59% reduction)
- At the dike (0 cm): solid ≈ 0.19, 3RC ≈ 0.05, fully porous ≈ 0.03 (~74% and ~84% reductions)
- Downstream (−5 cm): solid ≈ 0.20, 3RC ≈ 0.19, fully porous ≈ 0.16 (differences diminish, yet fully porous remains ~20% lower)

The strongest attenuation occurs at the structure, where bleed flow and distributed resistance suppress high-rotation cores and reduce their near-bed effectiveness—consistent with reduced scour and more stable deposition.

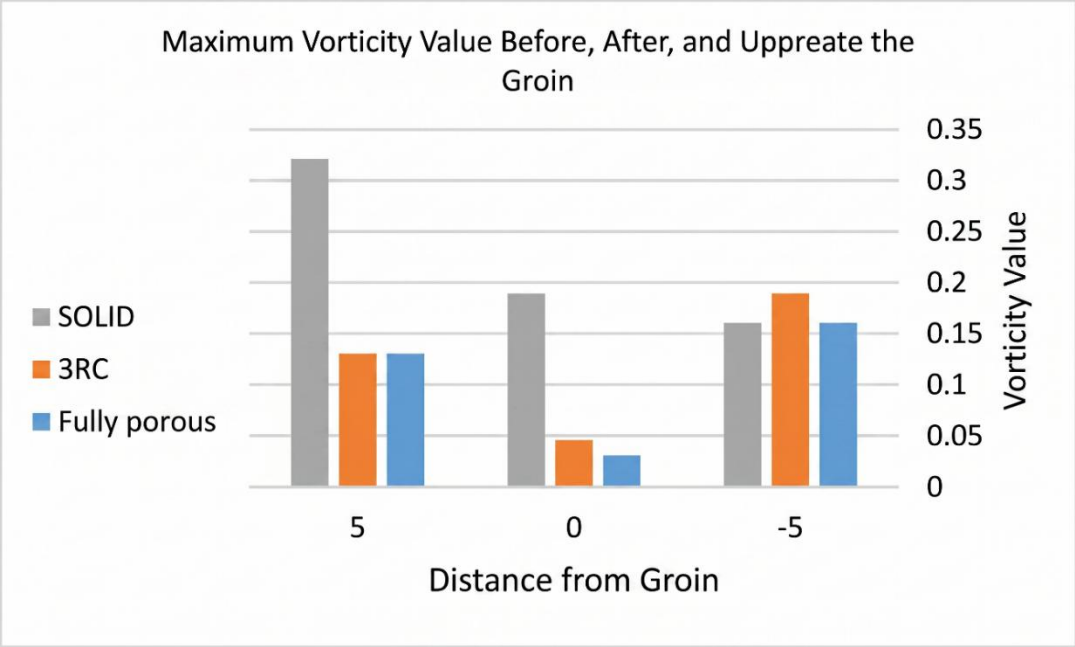

Figure 10- Maximum vorticity magnitude upstream of (+5 cm), at (0 cm), and downstream of (−5 cm) the spur dike for the three configurations.

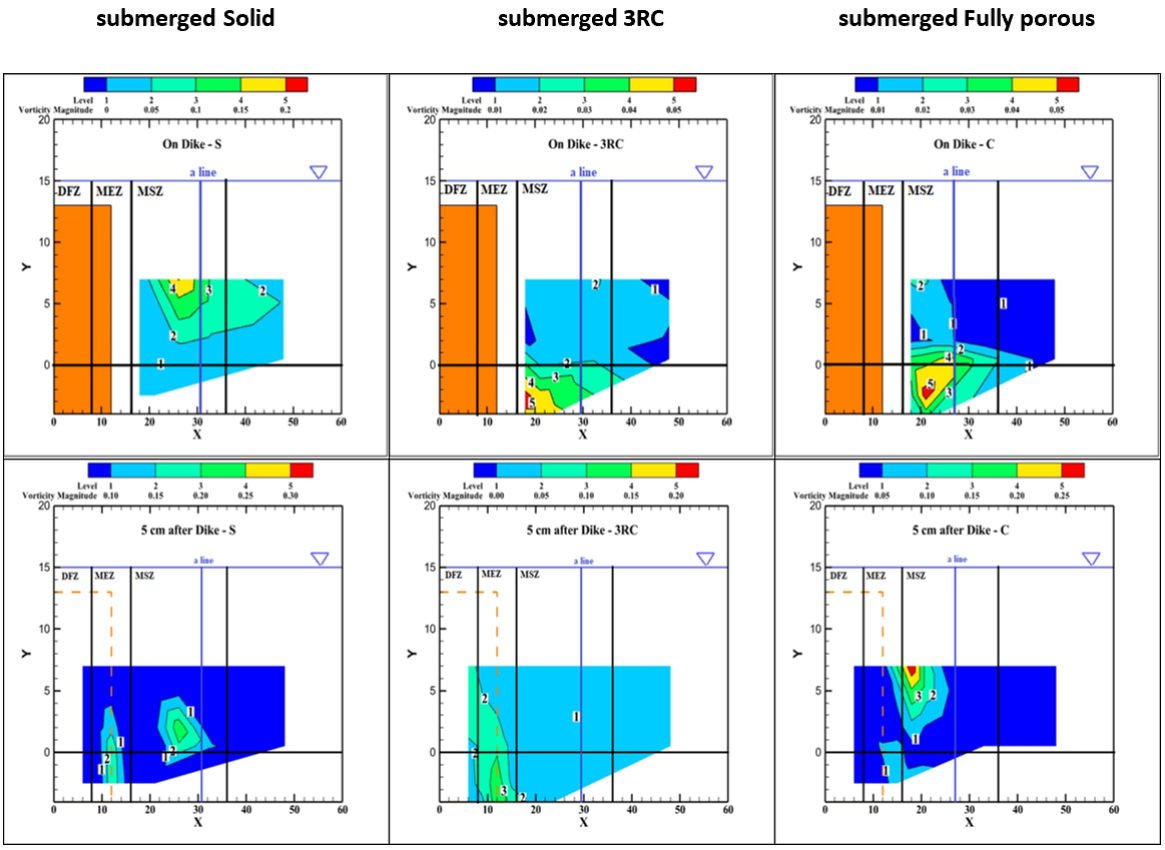

Figure 11- Vorticity-magnitude contours at the spur-dike section and 5 cm downstream under submerged conditions, comparing the three configurations.

3.6. Flow regions and qualitative observations (ADV + dye/yarn visualization)

To clarify the mechanisms underlying the ADV-based differences, velocity-magnitude patterns in Fig. 12 are interpreted together with dye injection and yarn tracers (Figs. 13–15).

Bleed flow and wake ventilation. A low-velocity signature in the DFZ–MEZ region (most evident for 3RC) is attributed to bleed flow through the pore network, which injects momentum into the low-pressure wake and alleviates strong suction and coherent reverse flow typical of impermeable dikes.

Suppression of the upstream dead-water region. The solid dike exhibits a distinct upstream stagnation/dead-water region (corresponding to Region II in Fig. 4). In the Chine configurations, this region is reduced, consistent with upstream pressure relief through the pores and weaker near-bed downflow.

Downstream displacement of dominant shear production under submerged flow. The interaction between crest-overtopping and bleed flow shifts the primary shear-production region downstream relative to the solid case, distributing velocity gradients over a longer reach and reducing the intensity of the near-tip shear layer.

Helical pathway and weaker surface boils. Yarn/dye tracking indicates a three-dimensional helical pathway after bed impingement, producing surface boils. In the porous cases—especially the fully porous dike—the reduced equilibrium scour depth leads to a smaller helical radius and weaker surface boils, consistent with reduced near-bed coherent activity.

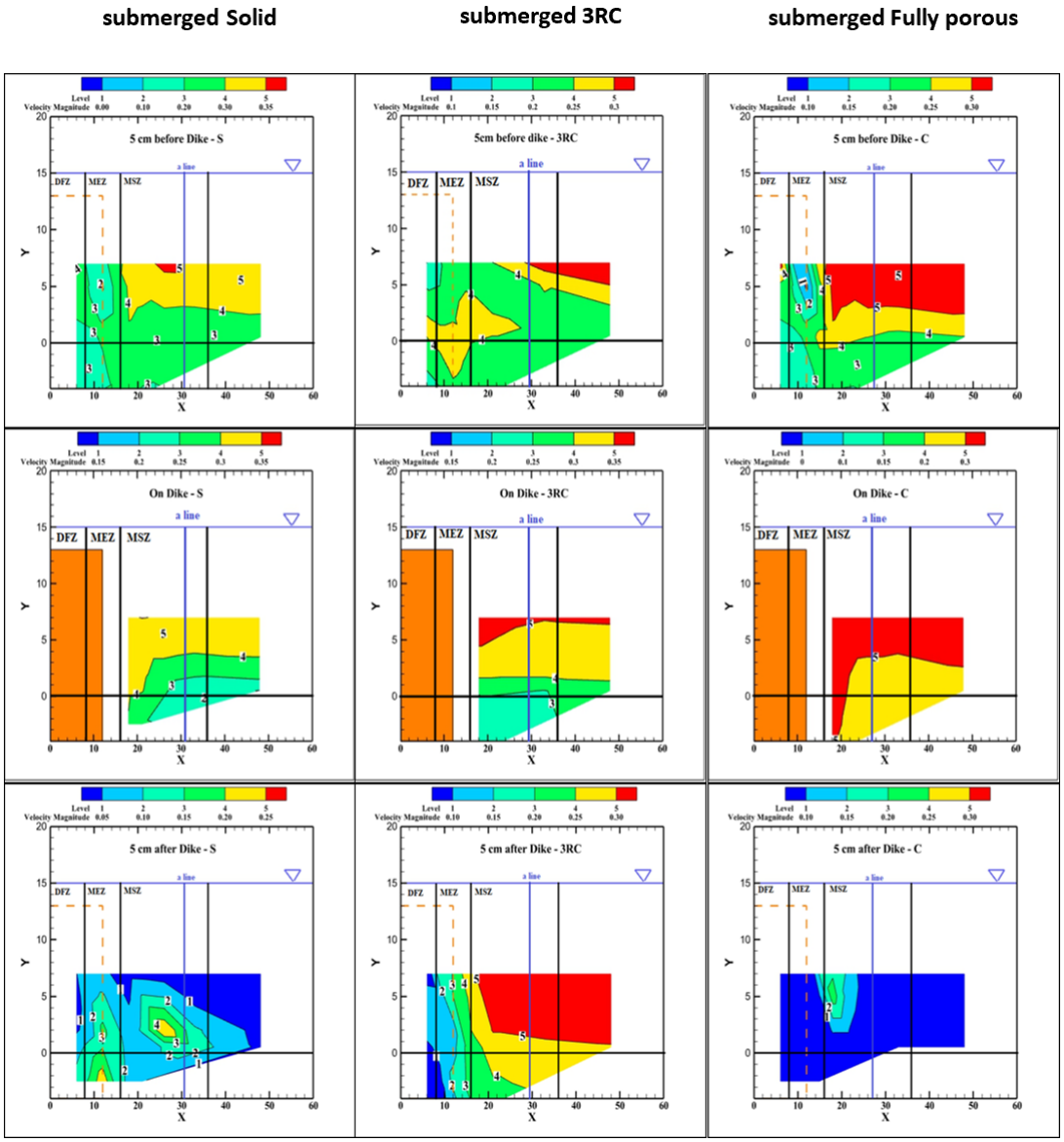

Figure 12- Velocity-magnitude contours (before, at, and after the spur dike) highlighting the bleed-flow signature in porous configurations.

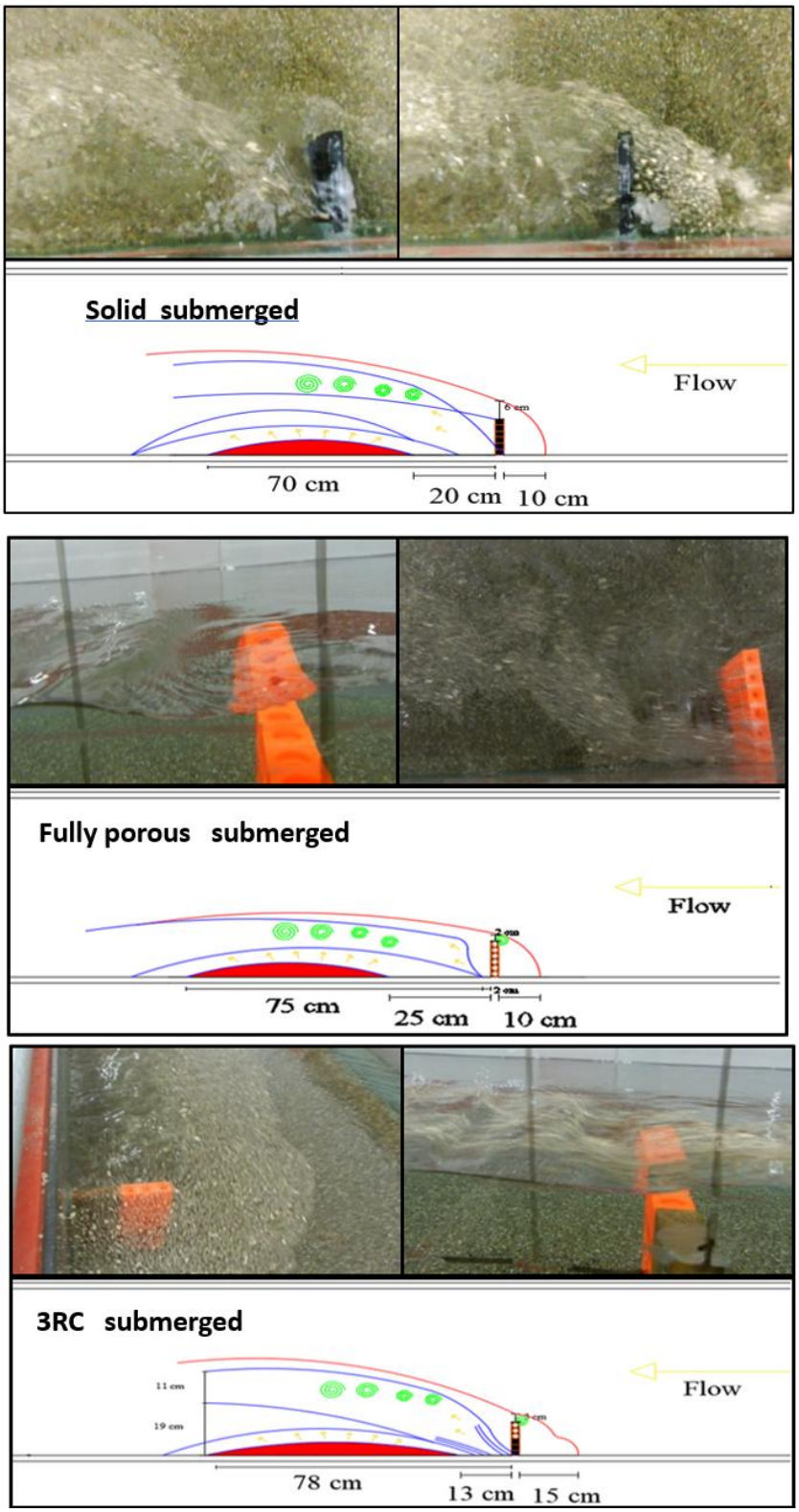

Figure 13- Schematic near-field velocity pattern around the spur dike under submerged conditions (based on ADV and visual observations).

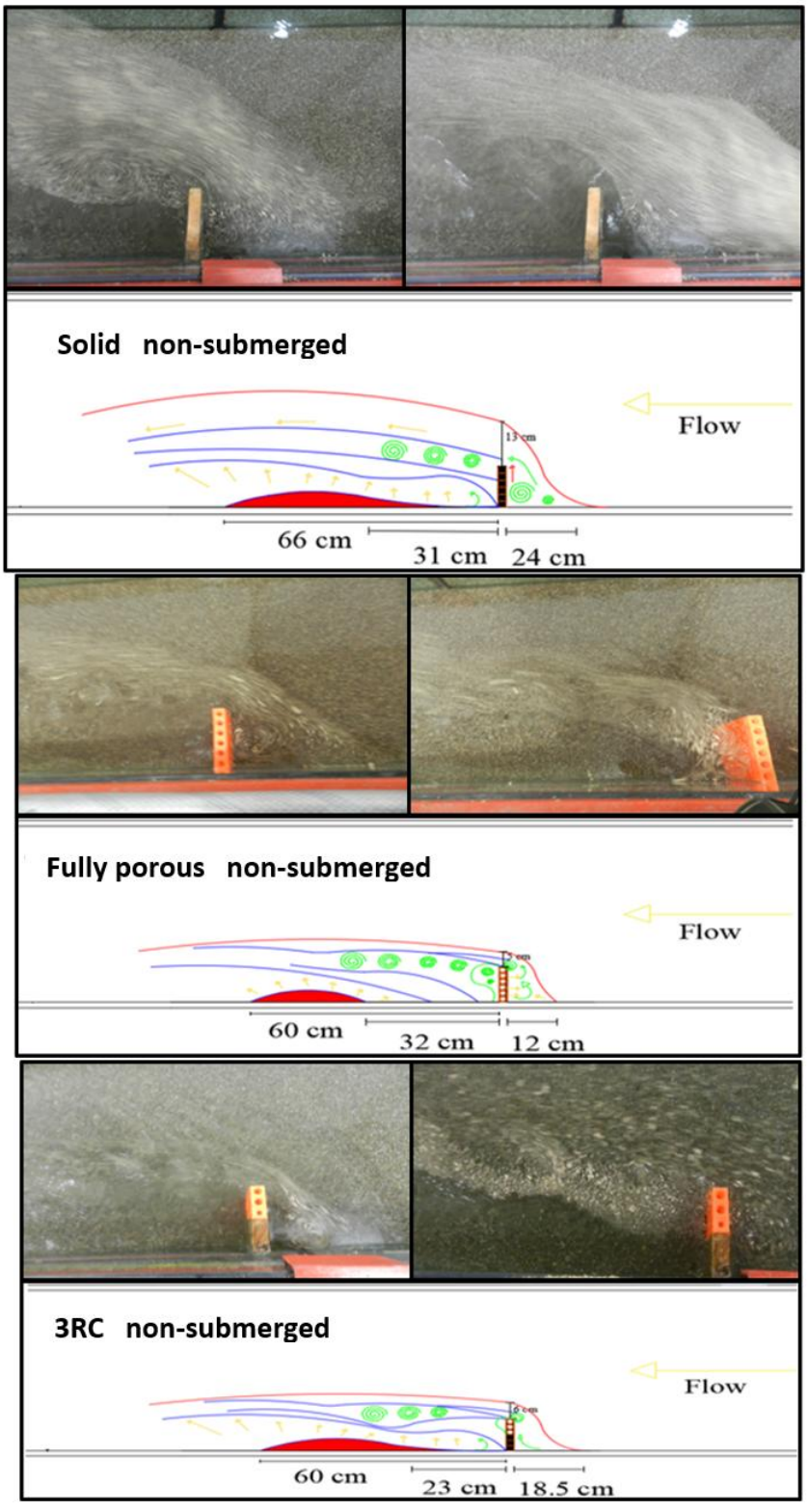

Figure 14- Schematic near-field velocity pattern around the spur dike under non-submerged conditions (based on ADV and visual observations).

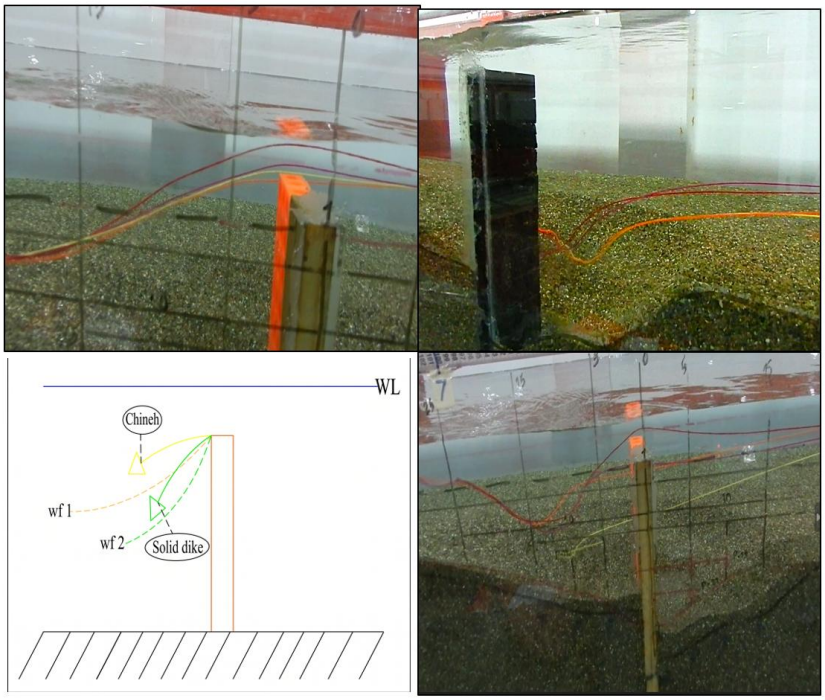

Figure 15- Conceptual sketch and visualization evidence of crest-overtopping flow (W_f) and its interaction with bleed flow for the submerged case, indicating downstream displacement of the dominant shear-production region.

3.7. Morphodynamic response and final bed topography (submerged and non-submerged)

Equilibrium bed topography provides the morphological fingerprint of flow–structure interaction. Figure 16 summarizes scour-hole descriptors (a, e, c, d, h_s) and deposition-bar onset distance; Figure 17 shows surveyed bed-elevation maps. The equilibrium maximum scour depth is:

$$d_s = | h_s | \tag{6}$$

3.7.1. Quantitative reduction of equilibrium scour depth

Under submerged conditions, the equilibrium scour depth is $d_s = 9.3$ cm for the solid dike, 7.1 cm for the fully porous Chine (23.7% reduction), and 8.2 cm for 3RC (11.8% reduction). Under non-submerged conditions, the corresponding scour depths are $d_s = 12.3$ cm (solid), 9.5 cm (fully porous; 22.8% reduction), and 11.7 cm (3RC; 4.9% reduction). With $h = 15$ cm and $L = 12$ cm, d_s/h decreases from 0.62 to 0.47 (submerged) and from 0.82 to 0.63 (non-submerged) for the fully porous Chine, consistent with the weakening of downflow and near-bed rotation documented in Sections 3.3 and 3.5.

3.7.2. Scour-hole geometry and inferred erosion mechanism

Beyond the reduction in maximum scour depth, the porous configurations significantly affected the overall geometry and footprint of the scour hole. Table 4 summarizes the equilibrium scour-hole dimensions extracted from the surveyed bed-topography maps shown in Figure 17.

Under submerged conditions, the impermeable spur dike generated the largest scour-hole footprint, with a maximum width (Ws) of 30.8 cm and a longitudinal extent (Ls) of 62.1 cm. In contrast, the fully porous Chine reduced these dimensions to 27.3 cm and 50.9 cm, corresponding to reductions of approximately 11% and 18%, respectively. The 3RC configuration exhibited intermediate behavior, with Ws = 29.9 cm and Ls = 54.0 cm.

A similar trend was observed under non-submerged conditions. The maximum scour-hole width and length decreased from 37.2 cm and 75.4 cm for the solid spur dike to 32.6 cm and 62.8 cm for the fully porous Chine, corresponding to reductions of approximately 12% and 17%, respectively. The 3RC configuration again produced intermediate values.

These results indicate that regular three-dimensional volumetric porosity not only mitigates local scour depth but also suppresses the lateral and downstream expansion of the scour hole. The observed contraction of the scour-hole footprint suggests that momentum redistribution through the interconnected pore network weakens the coherent erosive structures responsible for concentrated bed excavation, leading to a more spatially distributed and hydraulically stable erosion pattern.

Table 4- Quantitative comparison of equilibrium scour-hole geometry for the tested spur-dike configurations.

Flow condition	Configuration	ds (cm)	Ws (cm)	Ls (cm)	ds/h
Submerged	Solid	9.3	30.8	62.1	0.62
	3RC	8.2	29.9	54	0.55
	Chine	7.1	27.3	50.9	0.47
Non-submerged	Solid	12.3	37.2	75.4	0.82
	3RC	11.7	35	69.5	0.78
	Chine	9.5	32.6	62.8	0.63

where ds is the maximum scour depth, Ws is the maximum scour-hole width, and Ls is the maximum longitudinal scour extent.

3.7.3. Deposition-bar stability and onset location

The deposition-bar onset distance (Fig. 16) reflects wake recovery and quiescence. Under submerged flow, onset is 23.2 cm for the solid dike, 14.95 cm for the fully porous case (35.6% closer), and 15.75 cm for 3RC (32.1% closer). Under non-submerged flow, onset distances are similar (24.5, 24.9, and 23.7 cm), suggesting that the main benefit of regular porosity in the non-submerged regime is expressed primarily through scour-depth reduction rather than a systematic shift in deposition onset.

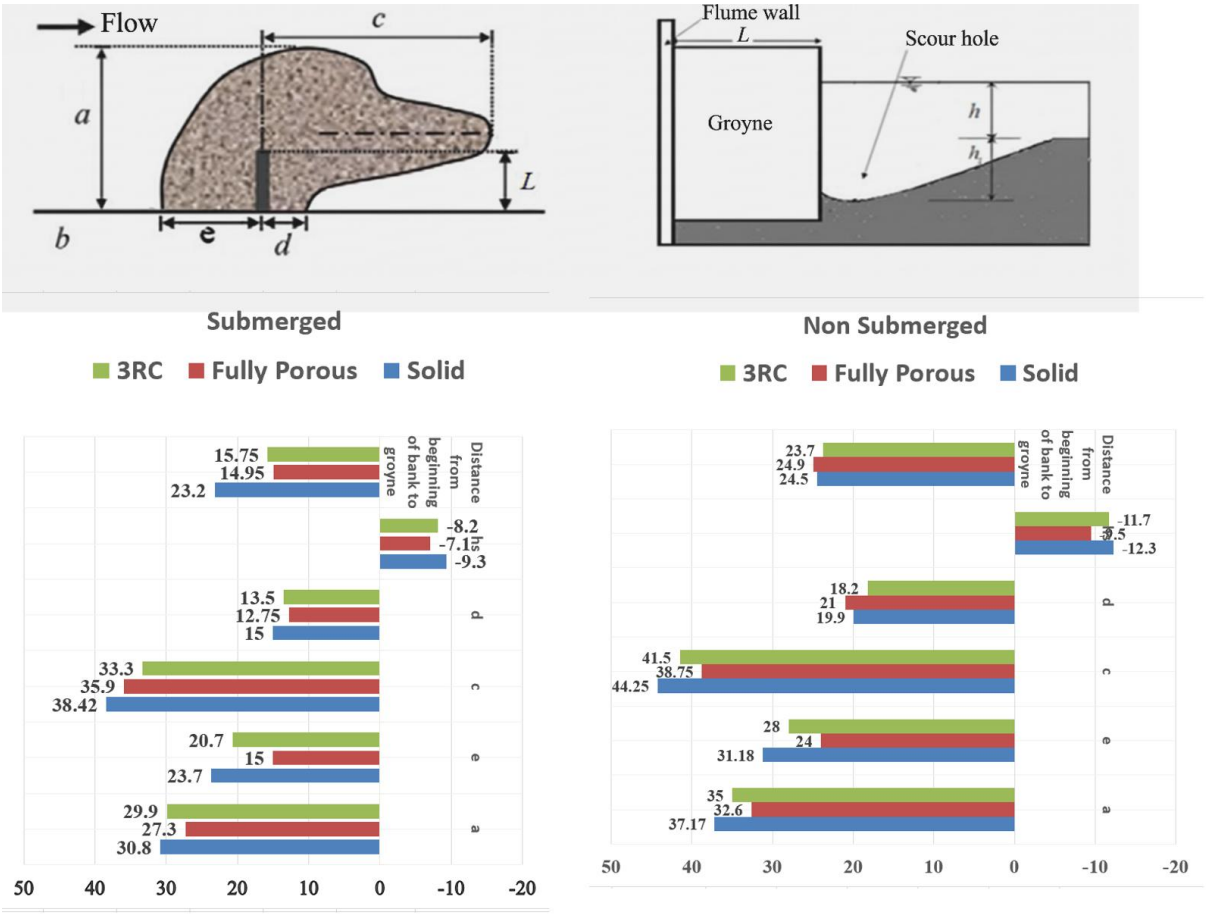

Figure 16- Equilibrium scour-hole geometric descriptors (a, e, c, d, h_s) and deposition-bar onset distance for submerged and non-submerged conditions (definitions of geometric parameters are shown in the inset).

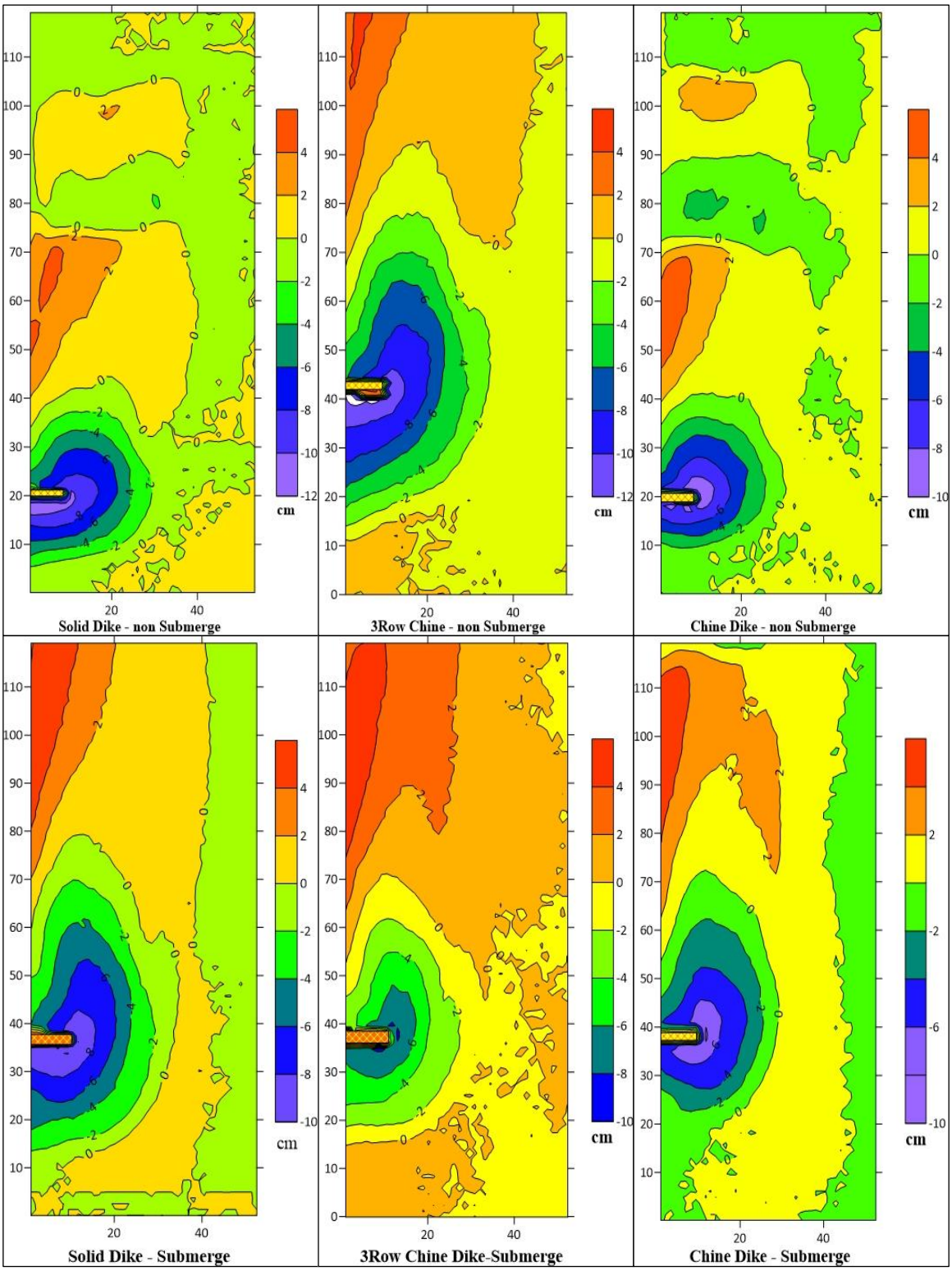

Figure 17- Measured equilibrium bed-elevation maps (laser profiler) around the spur dikes for submerged and non-submerged conditions (solid, 3RC, and fully porous Chine cases).

4. Discussion

Local scour around spur dikes remains one of the most critical challenges in river training and bank protection. The present study introduces a novel modular spur dike system based on regular, connected three-dimensional volumetric porosity (Chine blocks) and evaluates its performance against conventional designs. This section positions the findings within the existing body of literature.

4.1. Comparison with impermeable spur dikes

Extensive prior research on impermeable spur dikes has consistently identified the horseshoe vortex system (HSV), intense near-bed downflow, and shear-layer/wake instabilities as the dominant mechanisms driving local scour (Koken & Constantinescu, 2008a, 2008b; Koken, 2011; Chen et al., 2022; Duan et al., 2009). These studies demonstrated that flow stagnation upstream of the structure generates a strong adverse pressure gradient, which produces a downward jet that rolls up into a coherent HSV. This vortex, together with periodic wake vortex shedding, significantly amplifies bed shear stress and turbulent kinetic energy near the bed, leading to deep scour holes at the dike nose and tip.

The solid (impermeable) reference case in the present experiments aligns closely with these established mechanisms. The observed strong near-bed downflow, high vorticity cores, and pronounced recirculation zones are consistent with the classic flow topology reported in the literature. The primary contribution of this study lies in demonstrating that the introduction of regular, connected 3D volumetric porosity systematically disrupts this sequence. By enabling controlled bleed flow, the Chine configuration relieves upstream stagnation pressure, weakens the downflow jet, reduces the strength and near-bed coherence of vortical structures, and promotes more gradual wake recovery. These modifications produced a consistent and reproducible reduction in equilibrium scour depth of approximately 23% (23.7% submerged and 22.8% non-submerged) relative to the solid case. Such quantitative, porosity-controlled mitigation under both flow conditions provides stronger mechanistic insight than many earlier empirical observations.

4.2. Comparison with pile dikes and other permeable structures

Pile dikes and similar structures with two-dimensional permeability have been widely studied as alternatives to impermeable designs (Wang et al., 2023; Indulekha et al., 2023). While these configurations can reduce overall blockage, they may generate concentrated jets through gaps, potentially creating secondary localized scour that offsets the intended benefits.

In contrast, the Chine concept employs fully three-dimensional and spatially connected porosity. This geometry distributes incoming momentum through a regular pore network rather than discrete openings, significantly lowering the potential for concentrated jetting. The experimental results support this distinction: the fully porous Chine exhibited smoother velocity

gradients, reduced peak lateral velocities, weaker near-bed vorticity, and more spatially uniform wake recovery (particularly under submerged conditions) compared with the solid case. Furthermore, the earlier onset of organized deposition (35.6% closer to the structure under submerged flow) indicates faster transition to a stable wake regime. These outcomes suggest that regular 3D volumetric porosity achieves a more effective and predictable redistribution of turbulent energy than conventional 2D permeable structures.

4.3. Comparison with gabion spur dikes

Gabion spur dikes represent another class of volumetrically porous structures that have received increasing attention (Al-Awadi et al., 2025). Although gabions can reduce scour relative to impermeable dikes through bleed flow, their hydraulic performance is governed by highly irregular and random internal pore geometry. This randomness complicates parameterization, leads to variable bleed-flow distribution, and makes systematic prediction of wake characteristics and scour morphology challenging.

The Chine system overcomes these limitations by utilizing geometrically regular and mathematically connected pores ($\phi \approx 0.25$). This engineered regularity enables more predictable pressure relief, uniform momentum injection into the wake, and repeatable suppression of coherent structures. The present results demonstrate clear advantages: consistent scour-depth reduction, shallower and more spatially distributed scour holes, and well-organized downstream deposition patterns (especially under submerged conditions). These improvements highlight the superiority of designed, regular 3D porosity over random volumetric porosity for achieving controllable and reliable hydraulic performance in river-training applications.

4.4. Overall scientific positioning and novelty

This study advances the field by moving beyond the traditional binary classification of "impermeable vs. permeable" toward a more nuanced understanding of porosity topology. While previous works have largely focused on the degree of permeability, the present work emphasizes the critical importance of geometric regularity and three-dimensional connectivity of the pore network. The Chine design functions as a distributed energy dissipator that systematically weakens the primary scour-generating coherent structures (HSV and wake vortices) without introducing new localized scour triggers commonly observed in other permeable systems.

The ~23% reduction in equilibrium scour depth, achieved reproducibly under both submerged and non-submerged conditions, combined with improved wake stability, positions regular 3D volumetric porosity as a promising engineered solution for sustainable river training. These findings complement recent calls for more predictable and scalable permeable structures (Hussein et al., 2025; Rahman et al., 2024) and provide high-resolution experimental data linking pore-scale flow modulation to reach-scale morphodynamic response.

5. Conclusions

This study experimentally investigated how a regular, connected three-dimensional volumetric porosity (Chine) modifies 3D flow structure and local scour around spur dikes. The main findings are:

1. Flow-regime modulation: Regular porosity generates sustained bleed flow, shifting the response from full blockage (solid) to controlled throughput, relieving stagnation pressure and ventilating the wake.

2. Suppression of scour drivers: Under submerged flow, near-bed downflow weakened from about $W_{\min} \approx -0.10$ m/s (solid) to -0.05 m/s (porous), i.e., ~50% reduction. Peak vorticity at the structure decreased from ~0.19 s-1 (solid) to ~0.03 s^{-1} in the fully porous Chine (~84% reduction) and ~0.05 s^{-1} in 3RC (~74% reduction).

3. Distributed dissipation and reduced shear-layer concentration: The pore network distributes momentum exchange, producing more gradual shear-layer development and improved pressure recovery, reducing the dominance of coherent wake structures.

4. Superior morphodynamic performance of fully porous Chine: Equilibrium scour depth decreased by 23.7% (submerged) and 22.8% (non-submerged) relative to the solid case, and submerged deposition-bar onset occurred 35.6% closer to the structure, indicating a more stable wake/deposition environment.

Overall, regular 3D volumetric porosity provides an effective hydraulic mechanism—via bleed flow and pressure relief—to weaken near-bed coherent structures and reduce equilibrium local scour risk. Future work should assess porosity ratio and pore-size effects, spur-dike series arrangements, sediment gradation, and uncertainty quantification using raw ADV outputs (including Reynolds stresses and turbulence metrics).

References

Abdi Chooplou, C., Ghodsian, M., Vaghefi, M. V., Kazerooni, S., Bodaghi, E., 2022. Experimental study of effect of flow drop height on downstream bed topography of Type-A trapezoidal piano key weir. Journal of New Approaches in Water and Environmental Engineering, 1(1):113-124. https://doi.org/10.22034/nawee.2023.345240.1009.

Al-Awadi, A. T., Hussein, H. A., Alshami, A. H., Abdulameer, L., Al-Dujaili, A. N., 2025. Investigating the morphological changes of scour hole around gabion spur dikes. Scientific Reports, 15(1):36192.

Aung, H., Onorati, B., Oliveto, G., Yu, G., 2023. Riverbed morphologies induced by local scour processes at single spur dike and spur dikes in cascade. Water, 15(9):1746.

Buffin-Belanger, T., Roy, A. G., 2005. 1 min in the life of a river: Selecting the optimal record length for the measurement of turbulence in fluvial boundary layers. Geomorphology, 68(1-2):77-94.

Chakravarty, S., Patel, H. K., Mohanty, B., Kumar, B., 2024. Review on different shapes of spurs and their effects on channel morphology. Water Practice & Technology, 19(1):241-262.

Chen, Y., Lu, Y., Yang, S., Mao, J., Gong, Y., Muhammad, W. I., Yin, S., 2022. Numerical investigation of flow structure and turbulence characteristic around a spur dike using large-eddy simulation. Water, 14(19):3158.

Duan, J. G., He, L., Fu, X., Wang, Q., 2009. Mean flow and turbulence around experimental spur dike. Advances in Water Resources, 32(12):1717-1725.

Ezzeldin, R., Saqr, A. M., Abd-Elmaboud, M. E., 2026. Hydro-morphologic variations induced by bandal-like structures for river bank protection. Water Resources Management, 40(3):120.

Farshad, R., Kashefipour, S. M., Ghomeshi, M., Oliveto, G., 2022. Temporal scour variations at permeable and angled spur dikes under steady and unsteady flows. Water, 14(20):3310.

Goring, D. G., Nikora, V. I., 2002. Despiking acoustic Doppler velocimeter data. Journal of Hydraulic Engineering, 128(1):117-126.

Hajiabadi, M., Ramezani, Y., Khozeymehnezhad, H., 2025. The effect of the dimension of the openings on the scouring of the permeable spur dike at different angles. Iranian Journal of Irrigation & Drainage, 19(2):325-340. (In Persian).

Hussein, I. H., Jamel, A. A. J., Irzooki, R. H., 2025. Environmental and hydraulic considerations in scour reduction around spur dikes: A comprehensive review. Sustainable Marine Structures, 7(3):117-135. https://doi.org/10.36956/sms.v7i3.2125.

Indulekha, K. P., Jayasree, P. K., Balan, K., 2023. Laboratory investigation of flow and turbulent characteristics around permeable and impermeable groynes in a strongly curved meandering channel. ISH Journal of Hydraulic Engineering, 29(5):581-591.

Jafari, R., Sui, J., 2024. Channel deformation around non-submerged spur dikes with different alignment angles under ice cover. Journal of Hydrology and Hydromechanics, 72(3):372-385. https://doi.org/10.2478/johh-2024-0014.

Khodakarami, H., Abbasi, S., 2022. Impact of establishment distance of permeable protective groyne on local scouring depth control of the nose on a series of vertical impermeable groynes. Irrigation and Water Engineering, 12(4):195-212. (In Persian).

Koken, M., 2011. Coherent structures around isolated spur dikes at various approach flow angles. Journal of Hydraulic Research, 49(6):736-743.

Koken, M., Constantinescu, G., 2008a. An investigation of the flow and scour mechanisms around isolated spur dikes. Part 1: The start of the scour process. Water Resources Research, 44(8):W08406.

Koken, M., Constantinescu, G., 2008b. An investigation of the flow and scour mechanisms around isolated spur dikes. Part 2: The final stages of the erosion and deposition process. Water Resources Research, 44(8):W08407.

Li, D., Shen, X., Cai, H., Cao, L., Li, X., Gao, W., Li, S., 2024. The influence mechanism of the submerged dikes on the three-dimensional hydrodynamic characteristics at the 90° confluence. Physics of Fluids, 36(8):085167. https://doi.org/10.1063/5.0206346.

Mashizi, V. K., Zolghadr, M., Fathi, A., Zomorodian, S. M. A., 2025. An experimental, numerical, and case study on spur dike design, shedding light on common design practices. KSCE Journal of Civil Engineering, 29(7):100228.

Melville, B. W., 1997. Pier and abutment scour: integrated approach. Journal of Hydraulic Engineering, 123(2):125-136.

Melville, B. W., Chiew, Y. M., 1999. Time scale for local scour at bridge piers. Journal of Hydraulic Engineering, 125(1):59-65.

Melville, B. W., Coleman, S. E., 2000. Bridge scour. Highlands Ranch, CO: Water Resources Publications.

Nath, D., Misra, U. K., 2017. Experimental study of local scour around single spur dike in an open channel. International Research Journal of Engineering and Technology, 4(6):2728-2734.

Niknam, A., Heidarnejad, M., Masjedi, A., Bordbar, A., 2025. Investigation of the effect of plate on reducing the scour around spindle-shaped bridge pier. Journal of New Approaches in Water and Environmental Engineering, 4(2):1-19. https://doi.org/10.22034/nawee.2025.503788.1133.

Pandey, M., Valyrakis, M., Qi, M., Sharma, A., Lodhi, A. S., 2020. Experimental assessment of erosion around a spur dike in a channel with different bed roughness. International Journal of Sediment Research, 36(1):17-28.

Rahman, M. M., Shampa, Haque, A., Nakagawa, H., Zhang, H., Rahman, A., Hore, S. K., 2024. Sediment management using bandal-like structures as a nature-based solution. Environmental Fluid Mechanics, 24(4):757-787.

Rajaratnam, N., Nwachukwu, B. A., 1983. Flow near groin-like structures. Journal of Hydraulic Engineering, 109(3):463-480.

Raudkivi, A. J., Ettema, R., 1983. Clear-water scour at cylindrical piers. Journal of Hydraulic Engineering, 109(3):338-350.

Singh, B., Minocha, V. K., 2025. Hybrid ensemble models for scour depth prediction around spur dikes. Measurement, 256:118277.

Teraguchi, H., Nakagawa, H., Muto, Y., Baba, Y., Zhang, H., 2008. Flow and sediment transport around impermeable or permeable groins. Proceedings of Hydraulic Engineering, 52:175-180.

Uijttewaal, W. S. J., 2005. Effects of groyne layout on the flow in groyne fields. Journal of Hydraulic Engineering, 131(9):782-794.

Vaghefi, M., Radan, P., Akbari, M., 2019. Flow pattern around attractive, vertical, and repelling T-shaped spur dikes in a mild bend using CFD modeling. International Journal of Civil Engineering, 17(5):607-617.

Wang, Y., Xu, W., Li, W., 2023. Experimental study on the influence of new permeable spur dikes on local scour of navigation channel. Sustainability, 15(1):570.

White, F. M., 2011. Fluid mechanics. 7th ed. New York: McGraw-Hill.

Zahiri, A., Meftah, M., 2023. Prediction of maximum scour depth at bridge piers in case of debris accumulation. Journal of New Approaches in Water and Environmental Engineering, 2(1):17-32. https://doi.org/10.22034/nawee.2023.353101.1015.